Supplementary information for

A theory of tip structure-dependent microtubule catastrophes and damage-induced microtubule rescues

Veronika V. Alexandrova, Mikhail N. Anisimov, Aleksandr V. Zaitsev, Vadim V. Mustyatsa, Vladimir V. Popov, Fazoil I. Ataullakhanov, Nikita B. Gudimchuk

Corresponding author: Nikita B. Gudimchuk

Email: ngudimch@gmail.com

This file includes:

- Supplementary Methods
- Figures S1 to S11
- Table S1

Other supplementary materials for this manuscript include the following:

- Videos S1 to S10

Supplementary Methods

Four-state Monte Carlo model of microtubule dynamics

Microtubule is modeled as an array of tubulin dimers, which are arranged into 13-protofilament 3-monomer start left-handed helical B-type lattice. Tubulin dimers can exist in one of the four states: curved GTP-bound, straight GTP-bound, curved GDP-bound, straight GDP-bound. Transitions between the states are described with nucleotide-dependent rate constants and implemented with the first-reaction Gillespie algorithm (1), according to the schematic depicted in Fig 1A. Briefly, at each modeling step we define a complete set of possible events, which can be grouped into five types:

i) Association events: tubulin dimers can associate with the tips of 13 protofilaments. Arriving subunits are in the curved GTP-state. The probability of the association is not dependent on the state of the subunit, on which the tubulin dimer lands:

$$k_{on} = k_{+}\, c_{tub} \qquad \text{(eq. 1)},$$

where k_{+} is the association rate constant, c_{tub} is the soluble tubulin concentration.

ii) Dissociation events: any curved tubulin dimer can break its longitudinal bond with any of its neighbors with the probability described with k_{off} constant:

$$k_{off} = k_{+} \exp\left(-\Delta G_{long}\right) \qquad \text{(eq. 2)},$$

where ΔG_{long} is the free energy of a longitudinal bond.

iii) Straightening events: the curved dimers at the origin of a curved protofilament (i.e. those dimers in the curved state, which are longitudinally connected to a dimer in the straight state) can transition to the straight state with the rate constant k_{str}. For simplicity, this constant is the same with zero or one lateral bonds. If the tubulin dimer has two lateral tubulin neighbors in the straight state, its straightening constant is slowed down by a factor λ. The lateral bonds are automatically considered formed when two neighboring dimers adopt straight conformations in the adjacent protofilaments.

iv) Bending events: straight tubulin dimers at the origin of the curved protofilament (i.e. those dimers, which have only one straight longitudinal neighbor) can transition to the curved state with the rate constant k_{bend}. Assuming a thermodynamic equilibrium, this constant is calculated as follows:

$$k_{bend} = k_{str}\exp\left(-(n\Delta G_{lat} + \Delta G_{bend})\right) \quad \text{(eq. 3)},$$

where ΔG_{lat} is the free energy of a lateral bond, n is the number of lateral bonds being broken (n = 0, 1 or 2), and ΔG_{bend} is the deformation energy, released upon tubulin relaxation to the bent shape. At the seam, each tubulin dimer of the first protofilament can laterally interact with up to two dimers of the 13-th protofilament, each contributing ½ of the full lateral bond.

v) GTP hydrolysis can occur with the rate constant k_{hydr} in any of the GTP-tubulin dimers, which are capped with another tubulin dimer in the straight state, but not in the curved state.

For each of the events, which are possible at a given computational step, a stochastic reaction time τ_i is calculated:

$$\tau_i = \frac{-\log(r_i)}{k_i} \quad \text{(eq. 4)},$$

where r_i is a uniformly distributed random number generated from the interval [0;1], k_i is the kinetic rate constant, characterizing the i-th event.
Next, the event, corresponding to the smallest τ_i is realized and the total simulated time t_i is updated accordingly:

$$t_i = t_{i-1} + \tau_i \quad \text{(eq. 5)}$$

Model calibration

In our four-state model the properties of a tubulin dimer in each nucleotide state are described by five parameters: the straightening rate constant k_{str}, the kinetic penalty for straightening of the lagging protofilament, λ, the longitudinal bond energy ΔG_{long}, the lateral bond energy ΔG_{lat}, and the bending energy ΔG_{bend}. These parameters can in principle be different depending on the nucleotide state of tubulins. In the GTP-state, tubulins are additionally characterized by the GTP hydrolysis constant k_{hydr} and by the association rate constant, k_+. The latter parameter is not considered for the GDP-state because we assume that the concentration of GDP in solution is negligible. In order to fully calibrate the model, we need to apply a sufficient number of independent constraints for all of these 12 model parameters. We have developed the following iterative algorithm of the calibration.

While our Monte-Carlo model is a conceptual extension of the Brownian dynamics model developed previously (2), the parameters between them are not directly transferrable for two reasons: (i) the Brownian model considers tubulins as monomers, not as dimers as we do here; (ii) in the Monte Carlo model tubulin is assumed to be only in a curved (0.4 rad/dimer) or a straight (0 rad/dimer) conformation without any transitional states. Despite this, we estimated the tubulin bending energy in the GTP-state based on the Brownian dynamic model: $\Delta G^T{}_{bend} = 2 * 87 \frac{\text{kcal}}{\text{mol rad}^2} * \frac{0.2\ \text{rad}^2}{2} = 6\ \text{kT}$, where 87 kcal/mol/rad^2 is the bending stiffness of the protofilament, selected to be within the range of previously estimated values (2). The exact value of the dimer bending energy should not affect microtubule stability, since the microtubule stability is determined by the balance between lateral energy and bending energy, rather than the bending energy alone. With $\Delta G^T{}_{bend}$ parameter fixed, we initialize a parameter set which provides a roughly correct microtubule assembly rate at 10 μM tubulin concentration. Given this initial parameter set, we vary the straightening rate constant and the lateral bond energy to determine the dependence of the model behavior on these parameters (Fig S1A). From this dependence, the following tendency is clear: the lower is the k_{str}, the higher is the energy difference between $\Delta G^T{}_{lat}$ and $\Delta G^D{}_{lat}$ needed to match the experimentally observed microtubule growth rate (2): v_{growth} = 18 nm/s and the experimentally observed shortening rate (3): v_{short} = -400 nm/s. The same parameter k_{str} also determines the steepness of the microtubule growth rate dependence on tubulin concentration (Fig S1B,C). From the graphs in Fig S1A an S1BC it follows that for a growing microtubule k^T_{str} should be at least 300 s^{-1} to enable a well-documented linear dependence of the growth rate on tubulin concentration in the experimentally observed range from 0 to 20 μM. Setting the tubulin straightening rate k_{str} = 300 s^{-1} for both nucleotide states of tubulin, would mean that an energy as small as ~0.5 kT would be enough to convert the microtubule from growth to shortening (Fig S1A). To eliminate this high sensitivity of the microtubule behavior on the lateral bond energy, we reduced the straightening rate constant at the GDP-tubulin interface to k^D_{str} = 50 s^{-1} and kept it constant throughout the calibration procedure, while k^T_{str} remained equal to 300 s^{-1}.

Keeping the GTP hydrolysis off, we then calibrate three model parameters: ΔG_{lat}, ΔG_{long} and k_+ using the experimentally observed dependence of microtubule assembly rate on tubulin concentration (2) and the dependence of the average length of curved protofilaments at microtubule tips on tubulin concentration (4).

At first, we set the association constant, k_+, to an arbitrary value and build heatmaps of microtubule assembly rate (Fig S1D) and the length of curved protofilaments (Fig S1E) at 10 μM tubulin. Next, using these maps, we select the regions in them, corresponding to the range of experimentally observed values at 10 μM tubulin. The intersection of these regions yields lateral and longitudinal energies for a chosen k_+. These parameters are further used to plot the dependence of microtubule assembly rate on tubulin concentration (Fig S1F). This algorithm is repeated for other values of the association constant until the results match the experimental data (Fig S1F). An analogous procedure is applied to find lateral and longitudinal bond energies for GDP-tubulins. The tubulin association rate constant, k_+, which we found optimal, is in good agreement with the recent studies by Mickolajczyk *et al*. (5) and Cleary *et al*. (6), but substantially slower than deduced in an older study (7).

To calibrate the remaining parameters: k_{hydr}, $\Delta G^D{}_{bend}$ and λ, we use a similar strategy. For convenience we introduce a variable: $\Delta\Delta G_{bend} = \Delta G^D{}_{bend} - \Delta G^T{}_{bend}$. Starting from the assumption that $\Delta\Delta G_{bend} = 0$ (the bending energy of the tubulin dimer is the same in both nucleotide states), and then incrementing it with 2 kT steps, we generate a heatmap of microtubule catastrophe frequencies and delay times after tubulin dilution upon microtubule growth at 10 μM tubulin concentration. The heatmaps are built as functions of the two other unknown parameters: k_{hydr} and λ for each $\Delta\Delta G_{bend}$ (Fig S3AB). Importantly, for every new combination of the parameters $\{\Delta\Delta G_{bend}, k_{hydr}, \lambda\}$, the whole procedure, described in Fig S1D-F, is repeated again in the narrow range of around the previously found values of ΔG_{lat}, ΔG_{long} and k_+ to make sure that those parameters are appropriately corrected. This is done to keep the microtubule growth rate, disassembly rate and the lengths of curved protofilaments during assembly and disassembly in the range of experimentally observed values. The dependences of microtubule catastrophe frequency as a function of tubulin concentration are then plotted against the experimental data for each set of parameters (Fig S3C). The parameter set, which best matches the experimental data, is selected as the outcome of the calibration procedure. For the sake of simplicity, we postulated that parameter λ is the same in the GDP state of tubulins.

With this calibration routine, the distribution of the microtubule lifetimes is a prediction of the model. We found that with high λ values, it happens to be non-exponential, consistent with experimental data. However, we note that, alternatively, one could use the shape of this non-exponential distribution, described with two parameters, to calibrate the model, while the dependence of catastrophe frequency (also described by two parameters) would be a model prediction. We chose the former strategy here because of the availability of published measurements for all microtubule dynamics parameters, obtained in consistent conditions (2).

Quantification of microtubule behavior in the simulations

Microtubule length in the simulation was determined as the median length of the straight parts of all microtubule protofilaments. We used the *median* rather than the *mean* metric to make the microtubule length measurement less sensitive to small groups of lagging or leading protofilaments, which are poorly detectable experimentally. Simulated dependences of microtubule length on time were processed with a Matlab script, using the *findpeaks* function, to determine transitions between phases of microtubule growth and shortening. The *Minpeakprominence* parameter was set to 200 nm, which is roughly equivalent to the experimentally detectable limit of microtubule length change.

The probability of microtubule rescues with artificially embedded nGTP-islands were examined as follows. Simulations were started from the following configuration: 5-μm-long microtubules consisted of only GDP-tubulin subunits except for one nGTP tubulin patch of a given size, which was positioned 2.5 μm away from the tip. The soluble tubulin concentration was set to 10 μM. For each configuration of the nGTP-island (3x4, 4x3, 4x4, 5x3 dimers), N = 100 independent simulations were launched and analyzed. To predict the distribution of rescues in case of randomly positioned nGTP tubulin patches, the simulations were carried out analogously, but instead of the 5-μm-long microtubules, we used microtubule lengths, distributed as in our experimental data in the conventional assay. For each of the N = 457 microtubule lengths, we randomly positioned one nGTP tubulin patch (5x3-dimers) on the microtubule and determined the positions of rescue if it occurred before microtubule depolymerization to the nucleating seed.

To characterize the configuration of the microtubule tip, we calculated its raggedness as the standard deviation of the straight parts of the protofilaments, and the tip extension, as the difference in the length of the straight parts between the longest and the shortest protofilaments. To identify 'lagging' protofilaments, we compared the extent, by which the length of individual protofilaments deviated from the mean values of the tip extension, observed in a reference simulation with all parameters unchanged but λ set to 1. If the difference between the length of the protofilament deviated from the mean tip extension of the reference

simulation by more than three standard deviations, the protofilament was called 'lagging'. Practically, in most cases this criterion was met if a protofilament was at least 50 nm shorter than the protofilament with the maximal length.

Microtubule growth fluctuations were characterized with an effective 'diffusion' coefficient, *D*, calculated by fitting the mean squared change of the microtubule length per time interval Δt with the following equation:

$$\langle \Delta L^2 \rangle \; = \; 2\, D\, \Delta \mathrm{t} \; + \; v^2\, \Delta \mathrm{t}^2, \qquad \text{(eq. 6)}$$

Here v is the average microtubule growth rate. The minimal time interval, Δt, was equal to 10 s, as in the published experimental data (6). The growth fluctuations were assessed in the simulations with 7 μM tubulin and with one of the two GTP hydrolysis rate constant values: k_{hydr} = 0.09 s^{-1} or 0 s^{-1}.

Estimation of the lateral activation energy barrier

The activation energy barrier of the lateral bond is not an explicit parameter of our model. However, it can be estimated from the ratio, λ, of the rate constants for protofilament straightening with one lateral bond and two lateral bonds. We assume that the total energy landscape of a tubulin dimer, interacting with one or two lateral neighbors, has two potential wells, separated with an activation barrier (Fig S5). The transition rate constant from the bent state to the straight state can be found using Kramers formula for the inverse mean first-passage time of the tubulin dimer jumping over the potential barrier (8):

$$k_{str} = \frac{\sqrt{U''(r_{max})U''(r_{min})}}{2\pi\gamma} e^{-\Delta U/kT} \qquad \text{(eq. 7)}$$

Here *U* is the total energy profile, representing the sum of the tubulin bending energy and one or two lateral bonds, U'' is the second derivative of *U*, r_{max} is the distance between the tubulins, corresponding to the top of the energetic barrier, r_{min} is the distance between the tubulins, corresponding to the energy minimum in the bent tubulin state, γ is the friction coefficient. In Figure S5 we depicted the energy landscape, adopting the shape of lateral tubulin-tubulin energy and tubulin bending energy from our previous work (9).
Employing the Kramers formula (eq. 7), we can obtain the following equation for λ:

$$\lambda = \frac{k_{str}^{I}}{k_{str}^{II}} = \frac{\sqrt{U_I''(r_{max})U_I''(r_{min})}}{\sqrt{U_{II}''(r_{max})U_{II}''(r_{min})}} e^{-(\Delta U_I - \Delta U_{II})/kT} = \frac{\sqrt{U_I''(r_{max})U_I''(r_{min})}}{\sqrt{U_{II}''(r_{max})U_{II}''(r_{min})}} e^{\Delta\Delta U/kT} \qquad \text{(eq. 8)}$$

Here $\Delta\Delta U = \Delta U_{II} - \Delta U_I$ is the activation energy barrier, added by the second lateral bond, index *I* is the related to the free energy landscape with one lateral bond, index *II* is related to the landscape with two lateral bonds. Hence $\Delta\Delta U$ can be expressed as:

$$\Delta\Delta U = kT \ln(\lambda) + kT \ln\left(\frac{\sqrt{U_{II}''(r_{max})U_{II}''(r_{min})}}{\sqrt{U_I''(r_{max})U_I''(r_{min})}}\right) \qquad \text{(eq. 9)}$$

The first term in eq. 9 depends on λ and it determines the major part of the activation energy. The second term is a minor correction, which we estimate to be ~ 0.3 kT, provided that the shape of the tubulin-tubulin energy landscape is similar to the one assumed in our previous Brownian dynamics simulations (ref (9) and Fig S5C). This gives us an estimate for the activation energy barrier about 5 kT. This is a lower estimate because we used a fairly conservative value of the k_{str}^{I} here, while in reality it could be faster (see Model calibration).

Microfabricating coverslips with pedestals.
The pedestals on the coverslips were produced using photolithography. We created an optical mask by applying a layer of positive electron resist onto a standard glass blank with a 100-120-nm-thick chromium masking layer. The mask was then exposed on the ZBA-20 electron-beam lithograph (Carl Zeiss Jena, Germany). After exposure and development of the resist, etching of chromium was carried out in a liquid etchant. The mask obtained in this way used as a photomask for the optical exposure of the samples. Coverslips with microfabricated structures were made from SU-8 3005 resist (Microcem Corp, USA) deposited with a spincoater onto a 180-μm-thick cover glass substrate. The application was carried out at the speed of 4000 rpm with further drying on a hot plate at 95 °C for 5-10 minutes. The thickness of the resist was selected experimentally by dilution with cyclopentanone (SU-8 2000 Thinner, Microchem Corp.). The exposure was carried out on a contact exposure unit EM-583 (USSR). Post exposure baking was

carried out on a hot plate at 95 °C for 2-3 minutes. Then the sample was developed in methoxypropyl acetate (1-Methoxy-2-propyl acetate) for 20-30 seconds and rinsed with isopropanol and additionally dried at 100 °C for 10 minutes.

EB1 protein purification

A genetic construct encoding human EB1 protein fused at the C terminus to the EGFP-6His tag was cloned into pET28a vector. Protein expression was induced at 18°C for ~22 h with 0.8 mM IPTG in E. coli Rosetta (DE3) cells. Bacterial cells were pelleted and re-suspended into a non-ionic detergent-based lysis solution (B-PER, Thermo Scientific), supplemented with 0.5 mg/ml lysozyme, 1 mM phenylmethylsulfonyl fluoride and Roche Complete Protease inhibitors cocktail. The mixture was incubated for 15 minutes at room temperature on a rocker. All next steps were carried out at 4°C. 10 ml of the Purification Buffer (50 mM Tris-HCl pH 7.6, 300 mM NaCl, 1 mM β-mercaptoethanol, 10 % glycerol) with 10 mM imidazole was added to the bacterial solution. The mixture was then centrifuged at 17,000 g for 20 min in a tabletop centrifuge (Eppendorf). Next, the supernatant was mixed with 4 ml Ni-NTA Agarose (Invitrogen) and incubated for 1 hour and then loaded on a flow column. The column was washed with 20 ml of the Purification Buffer, supplemented with additional 30 mM imidazole, to remove non-specifically bound proteins. Next, the EB1-EGFP-6His protein was eluted into 1 ml fractions by washing the column with 5 ml of the Purification Buffer, supplemented with 200 mM imidazole. Two peak fractions of EB1-EGFP-6His were combined and loaded onto a PD-10 desalting column (Sigma Aldrich) pre-washed with BRB80 buffer with 10 % glycerol. The resulting protein solution was filtered through an ultrafiltration unit with 200 kDa molecular weight cutoff (Advantec USY-20) to remove possible aggregates, aliquoted, snap-frozen in liquid nitrogen and stored at -80°C before use.

Imaging microtubule dynamics in vitro

Observations of microtubule dynamics in the assays with the regular silanized coverslips or the coverslips with the microfabricated pedestals were carried out according to the protocol described in (10) with additional optimizations. Briefly, a flow chamber of a custom design, described previously (11), was mounted on a Nikon Eclipse Ti microscope equipped with an Andor iXon3 EMCCD camera and a 1.49NA TIRF 100x objective. The objective temperature of 32°C was kept constant using a heating collar (Bioptechs). Anti-digoxigenin antibodies (Roche Applied Science, 11093274910) diluted tenfold in BRB-80 buffer (80 mM K-PIPES, 1 mM MgCl2, 1 mM EGTA, pH = 6.8), added to the flow chamber using a syringe pump and incubated for 15 minutes. Then the chamber was washed with the BRB-80 buffer and a solution of 1% Pluronic F-127 was added, followed by incubation for 7 minutes in order to block nonspecific interactions with the coverslip. After that, the chamber was again washed with the BRB-80 buffer, and then a solution containing stabilized digoxigenin-labeled GMPCPP-tubulin seeds was added in order to immobilize them on the surface of the coverslip. Upon reaching the desired density of the seeds on the glass, the flow chamber was washed with the Image Buffer at the flow rate of 150 µl/min for the purpose of removing unattached seeds from the chamber. The Image Buffer (BRB-80 buffer supplemented with 1 mM GTP, 1 mM $MgCl_2$, 1 mM EGTA, 5 mg/ml bovine serum albumin, 0.08 mg/ml catalase, 0.1 mg/ml glucose oxidase, 12 mg/ml glucose, 1 mM dithiotrietol, 0.5 % β-mercaptoethanol) was centrifuged for 15 min at 25,000 g at 4 °C before introducing to the chamber. Next, a solution of 17 µM unlabeled tubulin in the Image Buffer was introduced into the chamber and microtubules dynamics were observed using DIC microscopy. In some experiments the solution was additionally supplemented with 100 nM EB1-eGFP-6His and 9 nM paclitaxel to induce more microtubule rescues (Fig S8CD, S9). Using a motorized XY-stage, 9-15 fields of view were selected, and then cyclically imaged for 30 minutes with an interval of 10-15 seconds and 100 milliseconds exposure. In the assay with the microfabricated pedestals, the experimental procedure was the same, except for the use of an additional 1.5X magnification in order to improve the quality of visualization of the microtubules.

Imaging GTP-tubulin incorporation into microtubule shaft

The experiments were carried out using the flow chambers assembled as described above. Alexa488-labeled (1 dye per 10 tubulin dimers) GMPCPP seeds were prepared and immobilized using the same protocols. 70-80 fields of view were pre-selected and imaged with DIC microscopy. Next, a solution of unlabeled 17 µM tubulin in the Image Buffer was added to the chamber for 7-8 minutes. Then, a solution containing 10 µM Alexa-488 tubulin (1 dye molecule per 3 tubulin dimers) in the same buffer with 2 mM GMPCPP instead of GTP was introduced to the chamber for 5-6 minutes to form stabilizing GMPCPP caps. After that, the chamber was washed with the Image Buffer. Next, a solution of 17 µM TAMRA-labeled tubulin (1 dye molecule per 1 tubulin dimer) in the Image Buffer with GTP was added to the chamber, followed by an incubation for 18-20 minutes to ensure the incorporation of free GTP-tubulins into the microtubule body. The chamber was then washed again with the Image Buffer. Addition of the labeled tubulins (Alexa-488,

TAMRA), as well as washes with the Image Buffer in this experiment at all stages occurred at 10 μL/min rate to ensure minimal deformation of the polymerized microtubules by the flow.

The fields of view pre-selected at the onset of the experiment were imaged sequentially at the final stage of the experiment in the DIC and two fluorescent channels: green (Alexa-488) and red (TAMRA). The green channel was used during analysis to identify microtubule boundaries. The DIC channel was helpful to make sure that Alexa488-labeled GMPCPP seeds and GMPCPP caps were correctly interpreted during analysis as parts of the same microtubule. The red channel was used to visualize tubulin incorporation into the microtubule shaft. In the pedestal assay, z-stacks (+/- 0.3 μm) were collected to improve sensitivity of the experimental setup for compensating z-plane fluctuations of the microtubule ends.

Pre-processing data to remove flare

Unprocessed images of microtubules in the assay with microfabricated pedestals have a strong flare at the edges of the pedestals in the DIC and in the fluorescence channels, impeding clear visualization of the microtubules. Therefore, we had to develop an algorithm to even the contrast around the pedestals. The algorithm was implemented as a set of scripts in ImageJ. The procedure starts from a shading correction followed by a slight rotation of each frame of the stack in order to orient the edges of the pedestals strictly vertically (Fig S6, Step I). Then, in the case of DIC, each stack is copied, one of the copies is shifted by 3 pixels vertically (along the pedestals); the other copy does not undergo additional transformations. The shifted stack copy is then subtracted frame by frame from its untransformed copy (Fig S6, Step II). In case of fluorescence, for each frame within one stack the intensities of all pixels in the vertical direction (along the pedestals) are averaged to produce a single intensity profile across the pedestals. Then, this averaged intensity profile is subtracted from each horizontal line of pixels in the corresponding frame. At the last step a copy of each stack is subjected to a Gaussian blur (sigma = 2) and subtracted from the unfiltered copy (Figure S6, Step II). Examples of data before and after application of the algorithm are shown in Fig S7. To make sure that this procedure does not affect the results of data analysis, we applied a similar algorithm to pre-process the data, obtained with the conventional coverslip-based assay.

Analysis of microtubule dynamics and GTP-tubulin incorporation into microtubule shaft in vitro

Pre-processed time-lapse stacks were further analyzed using ImageJ to quantify microtubule dynamics or incorporation of GTP-tubulin into microtubule shaft. First, using the DIC channel, we selected the microtubules, which did not intersect with each other and with other obstacles. Among these microtubules, we selected for further analysis those that did not exhibit any signs of non-specific sticking to the coverslip, as judged by the presence of microtubule fluctuations in the image plane or in the z-direction. In case when multiple solutions were introduced into the chamber throughout the experiment, we additionally made sure to avoid analysis of the microtubules, which experienced significant bending by the flow or those microtubules, which appeared to come in contact (for more than 3 consecutive frames) with any microtubule fragments, spontaneously nucleated in solution at the stage of the microtubule capping in the presence of GMPCPP in solution.

To quantify microtubule dynamics in the DIC channel, we used a custom script written in the Java language to plot a kymograph of each microtubule, which met the above criteria. The kymographs were used to determine the parameters of dynamic instability of the microtubules, i.e. the assembly rates, the positions and frequencies of rescues, microtubule lengths and catastrophe frequencies (Figure S8). The "plus" ends of the microtubules were distinguished from the "minus" ends by the faster assembly rates of the former. For each kymograph, we only processed those cycles of assembly and disassembly, which could be unambiguously interpreted. The time of observation was corrected accordingly. Microtubule growth rate was determined from the slope in the kymograph for each clearly visible assembly-disassembly cycle. Rescues and catastrophes were defined as transitions in microtubule dynamics, which were followed by elongation or shortening for at least 0.5 μm (3-4 pixels, depending on the magnification), respectively. We did not quantify rescues, which occurred within 0.5 μm from the nucleating seeds. We note, though, that elimination of such event was not the cause of the non-exponential distribution of rescue positions, as the peak of rescue locations was located significantly farther than 3-4 pixels from the seed. The frequency of rescues was defined as the ratio of the total number of rescues to the total time of observed depolymerization. Statistical analysis was performed, using the Prism GraphPad 8 software, applying a two-sided unpaired t-test.

Quantification of the GTP-tubulin incorporation into the microtubule shaft was carried out using a set of custom scripts in Matlab 2017b. A vector, defining the position of a microtubule was specified manually in the image from the green fluorescent channel (for the pedestal assay we used a maximal projection of the z-stack containing images of Alexa-488-labeled microtubule seeds and caps). This vector was by mouse-

clicking on the Alexa-488-labeled microtubule seed and the Alexa-488-labeled GMPCPP-tubulin cap. An intensity linescan along this vector in the red (TAMRA) channel was plotted in each of the three planes of the z-stack and smoothed with the *imgaussfilt* function (sigma = 2 for the pedestal assay and sigma = 1.5 for the conventional assay). The peak intensity was then fitted with a Gaussian curve; the height and the width of this fit were reported as the characteristics of the incorporated TAMRA-labeled GTP-tubulin islands. We considered the TAMRA-labeled profile as an incorporated island if its «prominence» was more than 3 standard deviations of the image noise and the width was at least 0.5 μm.

Sensitivity of TAMRA-tubulin islands detection

To make sure that the observed low rate of TAMRA-labeled GTP-tubulin incorporation into microtubule shaft in the pedestal assay was not an artifact of a lower sensitivity of the fluorescence detection in that assay compared to the conventional assay, we compared our ability to detect signal from TAMRA-labeled GMPCPP caps. Briefly, microtubules were polymerized from GMPCPP seeds and capped in the presence of TAMRA-labeled GMPCPP-tubulin with variable labeling densities (20, 30 and 50%) in the conventional or in the pedestal assay (Fig S10C). After that, we processed the data as described in the previous section to quantify the intensities of the TAMRA-labeled GMPCPP caps. As illustrated in Fig S10D, the intensity of the signals, corresponding to the TAMRA-labeled caps, were comparable in both assays. We fit the dependence of the TAMRA-labeled GMPCPP caps on the labeling degree of the cap with the following function (solid lines in Fig S9D):

$$Y = A\frac{X}{X\left(k_{on}^{TAMRA}-k_{on}^{unlabeled}\right)+\alpha\, k_{on}^{TAMRA}} \qquad \text{(eq. 10)}$$

Here X is the density of the cap labeling; α is the labeling degree of TAMRA-tubulin, which is mixed with unlabeled tubulin in our assay to vary the density of the cap labeling; k_{on}^{TAMRA} is the association rate constant for TAMRA-tubulin, $k_{on}^{unlabeled}$ is the association rate constant of unlabeled tubulin, *A* is a coefficient, defined by the imaging settings.

The signal detection sensitivity determined as the intensity equal to the standard deviation of the background noise, corresponded to the degree of labeling with TAMRA-tubulin about 5% in both the conventional and the modified assays. The cap sizes in these control experiments were comparable to the sizes of the GTP-tubulin islands, incorporating into microtubule shafts (Fig S10E), suggesting that the detection limit should be similar and sufficient to detect TAMRA tubulin islands of similar sizes in our conventional and pedestal assays.

Supplementary references

1. D. T. Gillespie, A general method for numerically simulating the stochastic time evolution of coupled chemical reactions. *Journal of Computational Physics* **22**, 403–434 (1976).

2. C. Strothman, *et al.*, Microtubule minus-end stability is dictated by the tubulin off-rate. *J. Cell Biol.* **218**, 2841–2853 (2019).

3. R. A. Walker, *et al.*, Dynamic instability of individual microtubules analyzed by video light microscopy: rate constants and transition frequencies. *J. Cell Biol.* **107**, 1437–1448 (1988).

4. J. R. McIntosh, *et al.*, Microtubules grow by the addition of bent guanosine triphosphate tubulin to the tips of curved protofilaments. *J Cell Biol*, jcb.201802138 (2018).

5. K. J. Mickolajczyk, E. A. Geyer, T. Kim, L. M. Rice, W. O. Hancock, Direct observation of individual tubulin dimers binding to growing microtubules. *Proc. Natl. Acad. Sci. U.S.A.* (2019) https:/doi.org/10.1073/pnas.1815823116.

6. J. M. Cleary, *et al.*, Measurements and simulations of microtubule growth imply strong longitudinal interactions and reveal a role for GDP on the elongating end. *eLife* **11**, e75931 (2022).

7. M. K. Gardner, *et al.*, Rapid Microtubule Self-Assembly Kinetics. *Cell* **146**, 582–592 (2011).

8. H. A. Kramers, Brownian motion in a field of force and the diffusion model of chemical reactions. *Physica* **7**, 284–304 (1940).

9. N. B. Gudimchuk, *et al.*, Mechanisms of microtubule dynamics and force generation examined with computational modeling and electron cryotomography. *Nature Communications* **11**, 3765 (2020).

10. A. E. Vartanova, *et al.*, Expanding Stereoelectronic Limits of endo-tet Cyclizations: Synthesis of Benz[b]azepines from Donor–Acceptor Cyclopropanes. *J. Am. Chem. Soc.* (2021) https:/doi.org/10.1021/jacs.1c07088 (August 20, 2021).

11. V. A. Volkov, A. V. Zaytsev, E. L. Grishchuk, Preparation of segmented microtubules to study motions driven by the disassembling microtubule ends. *J Vis Exp* (2014) https:/doi.org/10.3791/51150.

12. C. Duellberg, N. I. Cade, T. Surrey, Microtubule aging probed by microfluidics-assisted tubulin washout. *MBoC* **27**, 3563–3573 (2016).

Table S1. Model parameters

Parameter name	Description	'high barrier' case	'low barrier' case
λ	Kinetic penalty for bent protofilament straightening in presence of two straight adjacent protofilaments	105	1
k_+	Tubulin association rate constant	0.55 $s^{-1}\mu M^{-1}$	0.3 $s^{-1}\mu M^{-1}$
k^T_{str}	GTP-tubulin dimer straightening rate constant with zero or one protofilament neighbor	300 s^{-1}	300 s^{-1}
k^D_{str}	GDP-tubulin dimer straightening rate constant with zero or one protofilament neighbor	50 s^{-1}	50 s^{-1}
ΔG^T_{long}	free energy of a longitudinal bond that a GTP tubulin forms with an adjacent dimer (trans)	-13.2 k_BT	-13.8 k_BT
ΔG^D_{long}	free energy of a longitudinal bond that a GDP tubulin forms with an adjacent dimer (trans)	-12.8 k_BT	-12.8 k_BT
ΔG^T_{bend}	the deformation energy of a straight tubulin dimer, connected to a given GTP-tubulin (trans)	6 k_BT	6 k_BT
ΔG^D_{bend}	the deformation energy of a straight tubulin dimer, connected to a given GDP-tubulin (trans)	8 k_BT	8 k_BT
ΔG^D_{lat}	free energy of a lateral bond that a GDP tubulin forms with an adjacent dimer (cis)	-5.6 k_BT	-5.6 k_BT
$\Delta G^{T,D/T}_{lat}$	free energy of a lateral bond that a GTP tubulin forms with an adjacent dimer (cis)	-7.5 k_BT	-8.5 k_BT
k_{hydr}	GTP hydrolysis rate constant	0.09 s^{-1}	0.43 s^{-1}

Supplementary Figures

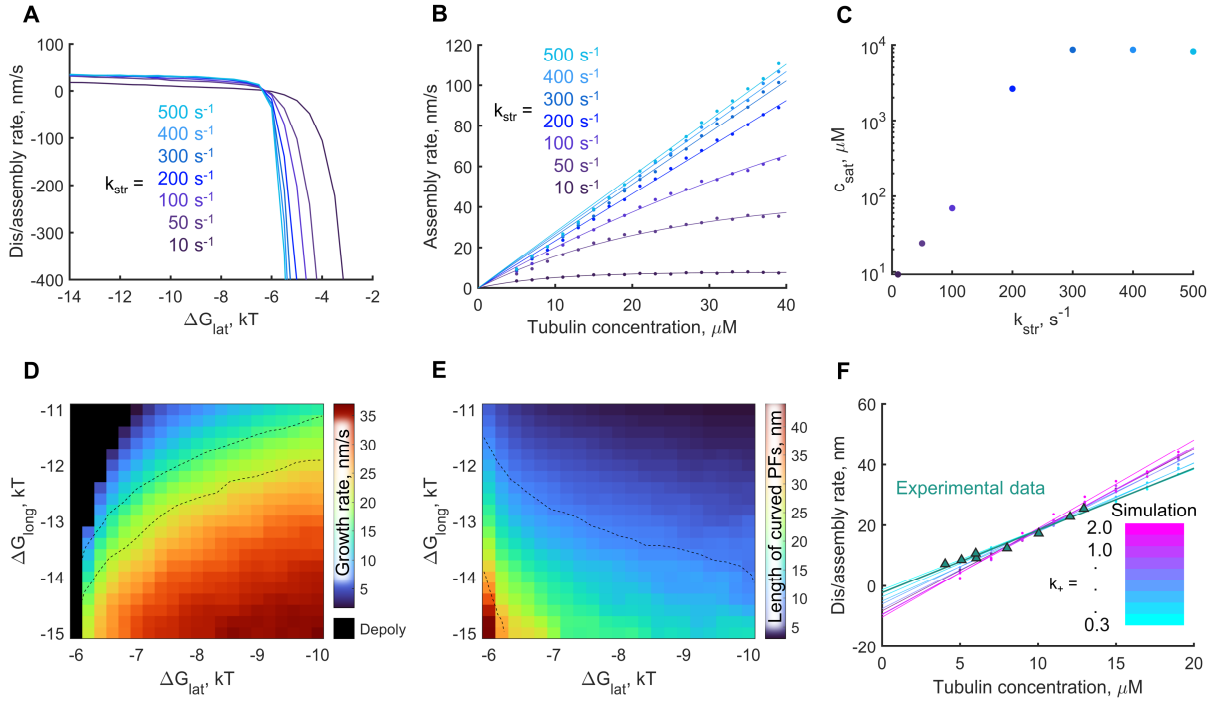

Figure S1. Calibration of the four-state model (tubulin bond energies, straightening and association rates) with the GTP hydrolysis turned off. (A) Dependence of the microtubule assembly rate (positive values) or disassembly rate (negative values) on the lateral bond energy for different tubulin straightening rate constants. (B) Microtubule assembly rate as a function of tubulin concentration for different tubulin straightening rate constants. Each point is a mean value from N = 5 individual simulations. Solid lines are data fits with an exponential function: $Y = Y_0 (1 - \exp(-c/c_{sat}))$. (C) Fitting parameter c_{sat} as a function of tubulin straightening rate constant. It is clear that c_{sat} reaches a plateau at k_{str} = 300 s^{-1}. Each point is a mean value from N = 5 individual simulations. (D) A heatmap of microtubule growth rates as a function of ΔG_{long} and ΔG_{long} at 10 μM tubulin concentration. Dotted lines mark the boundaries of the region, corresponding to experimental values: 18 ± 3 nm/s (2). (E) A heatmap of the average length of curved protofilaments rates at the microtubule tip as a function of ΔG_{long} and ΔG_{lat} at 10 μM tubulin concentration. Dotted lines mark the boundaries of the region, corresponding to experimental values: from 15 to 40 nm (4). (F) Microtubule growth rates vs. tubulin concentration for different tubulin association rate constants (k_+ is varied in the range from 0.3 to 2.0 $\mu M^{-1}s^{-1}$). For each line ΔG_{long} and ΔG_{lat} are pre-calibrated (see the heatmaps in panels D, E) so that microtubule growth rate and the length of curved protofilaments match experimental data at 10 μM tubulin concentration.

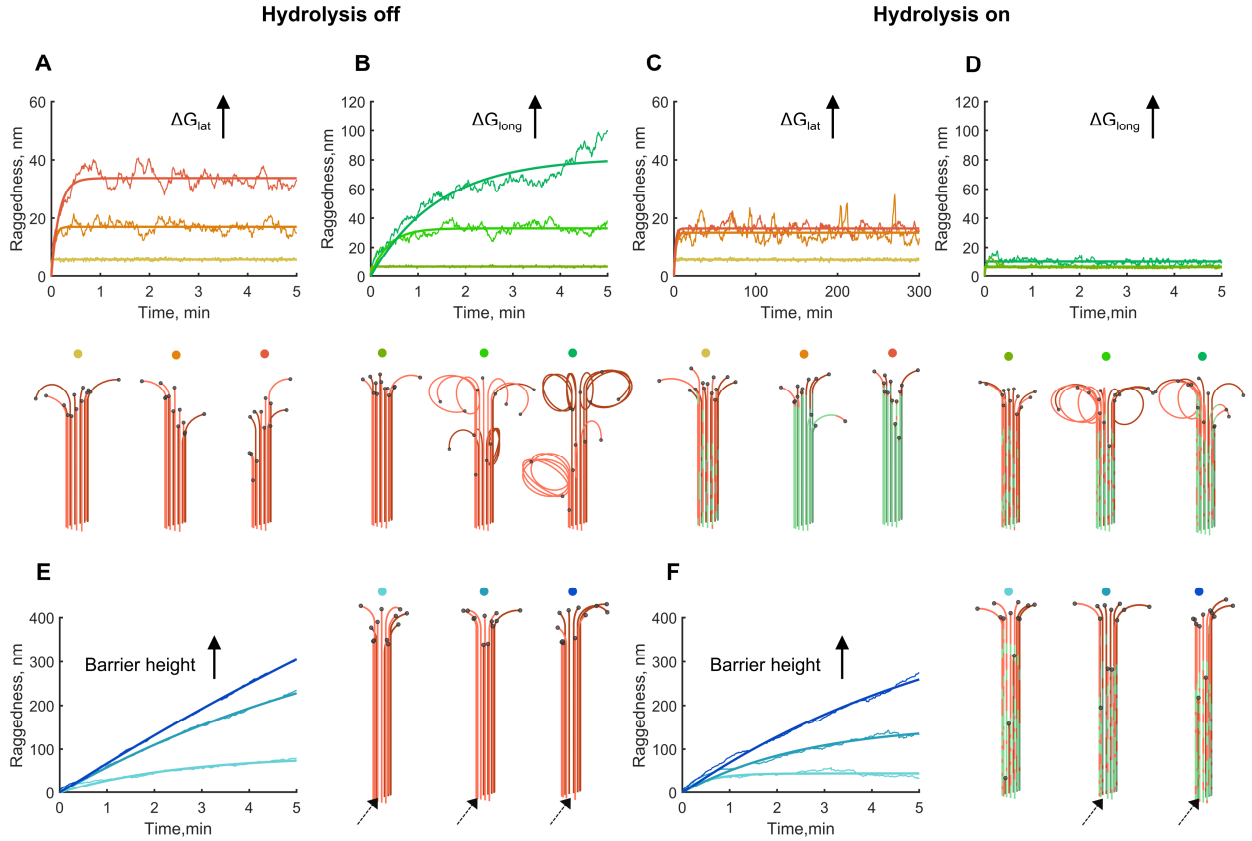

Figure S2. Analysis of microtubule tip raggedness as a function of model parameters. (A) Upper part of the panel: dependence of microtubule tip raggedness on time for different lateral bond energies. (ΔG_{lat} = -7, -11, -15 kT). Raggedness is quantified as the standard deviation of the lengths of straight parts of the protofilaments. Lower part of the panel: example images of microtubule tips, corresponding to parameter sets color coded (see a colored dot above each microtubule) as the curves in the graph above. Black dots mark the termini of the protofilaments to make each protofilament's tip more clearly visible. (B) Upper part of the panel: dependence of microtubule tip raggedness on time for different longitudinal bond energies: ΔG_{long} = -13, -19, -25 kT. Lower part of the panel: example images of microtubule tips, corresponding to parameter sets color coded as the curves in the graph above. (C) and (D) are the same as panels A and B, respectively, with GTP hydrolysis on. (E) On the left: dependence of microtubule tip raggedness on time for different activation energy barriers (λ = 90, 105, 120). On the right: example images of microtubule tips, corresponding to parameter sets color coded as the curves in the graph on the left. (F) Same as panel E with GTP hydrolysis on. Black arrows point at the missing protofilaments, whose tips are lagging beyond the image. In all panels every curve is an average of N = 30 simulation runs. Solid smoother lines are fits with exponential functions: $Y=Y_0(1 - \exp(-X/X_0)$.

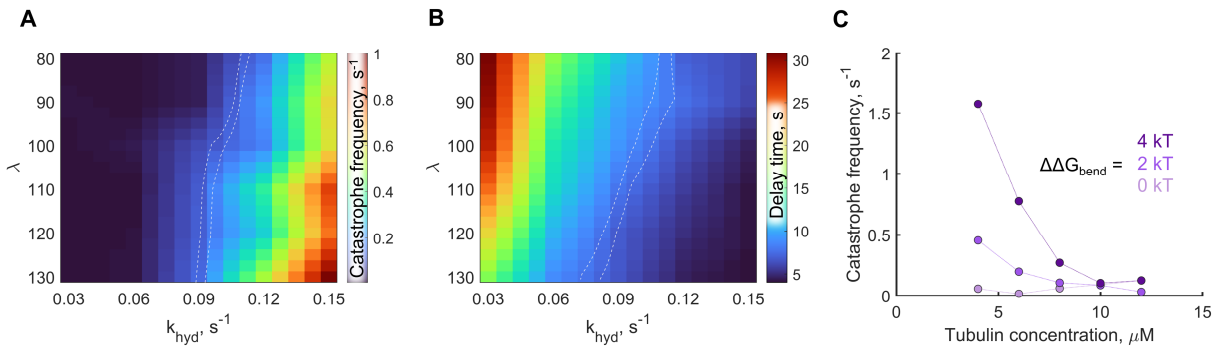

Figure S3. Calibration of the four-state model (GTP hydrolysis rate, kinetic penalty for straightening of lagging protofilaments and bending energies of GTP and GDP tubulins). (A) A heatmap of microtubule catastrophe frequency as a function of k_{hydr} and λ at 10 μM tubulin concentration. The heatmap was computed with 4-fold lower resolution and interpolated. Dotted lines mark the boundaries of the region, corresponding to experimental values: 0.09 ± 0.01 s^{-1} (2). (B) A heatmap of the delay times after tubulin dilution till catastrophe as a function of k_{hydr} and λ at 10 μM tubulin concentration. The heatmap was computed with 4-fold lower resolution and interpolated. Dotted lines mark the boundaries of the region, corresponding to experimental values: 8.5 ± 0.5 s (2, 12). (C) Microtubule catastrophe frequency vs. tubulin concentration for different $\Delta\Delta G_{bend} = \Delta G^{D}_{bend} - \Delta G^{T}_{bend}$ ($\Delta\Delta G_{bend}$ is varied in the range from 0 to 4 kT). For each line, k_{hydr} and λ are pre-calibrated so that microtubule catastrophe frequency and the delay time after tubulin dilution match experimental data at 10 μM tubulin concentration.

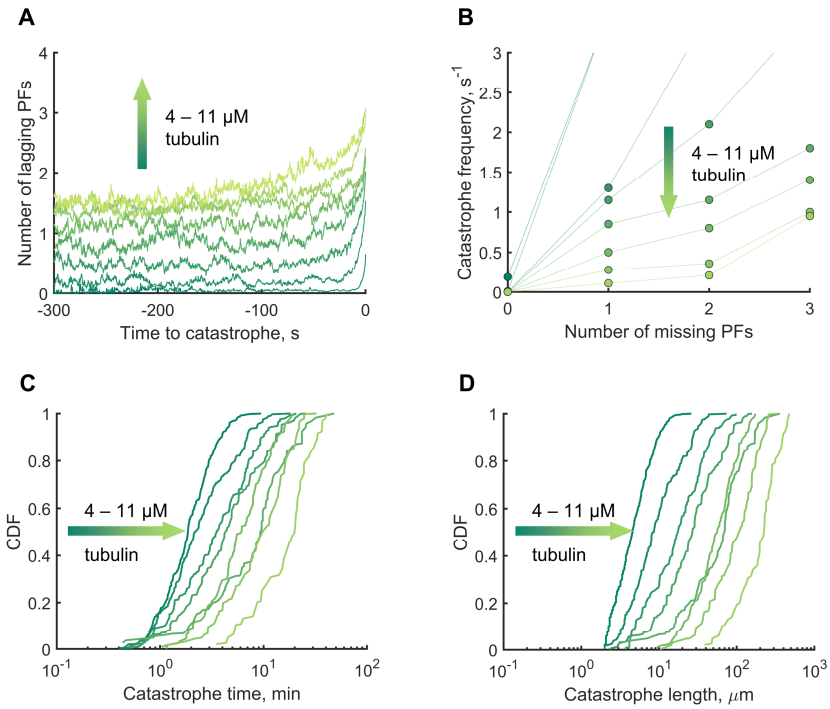

Figure S4. Microtubule aging driven by accumulation of the lagging curved protofilaments at the growing tip. (A) Number of lagging protofilaments as a function of time before catastrophe. The higher is the tubulin concentration, the more lagging protofilaments is required to destabilize the microtubule growth. (B) Dependence of catastrophe frequency on the number of missing protofilaments (the elongation of these protofilaments is artificially blocked in the simulation). Each curve in panels A-B is based on 1000 min of the simulated time. (C) Cumulative distribution functions (CDF) for catastrophe times in the simulations with different tubulin concentrations. (D) Cumulative distribution functions for microtubule lengths at the times of catastrophes in the simulations with different tubulin concentrations.

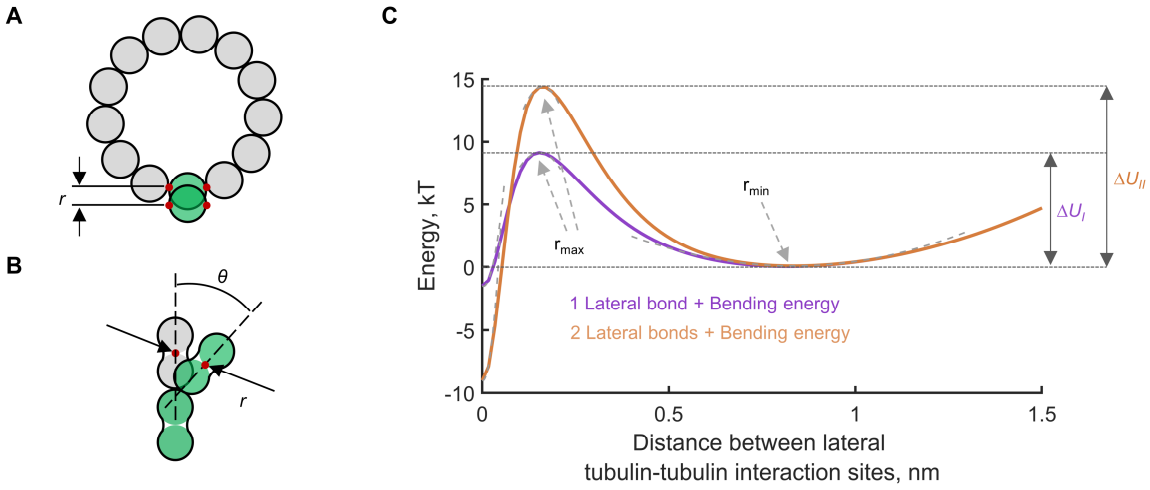

Figure S5. Estimation of activation energy barrier from the kinetic penalty for the straightening of lagging protofilaments. (A) Schematics of a lagging protofilament (green), surrounded by straight protofilament neighbors (gray). Microtubule is shown in crossection. *r* is the distance between the lateral tubulin-tubulin interactions sites. (B). The same protofilament is shown from the side. θ is the bending angle; *r* is the distance between the lateral sites of bent and straight tubulins. (C) Hypothetical energy landscape resulting from summing tubulin bending energy profile 1 lateral bonds with straight neighbors (purple curve) or with 2 lateral bonds with straight neighbors (orange curve). The energy landscape is plotted as a function of the distance between the lateral sites of bent and straight tubulins, *r* (see panels A and B). r_{min} is the tubulin separation distance, corresponding to the bent state of tubulin. r_{max} is the tubulin separation distance, corresponding to the top of the activation energy barrier. ΔU_I and ΔU_{II} are the activation energy heights for the pathway from bent to straight state of tubulin in case of one and two lateral bonds, respectively.

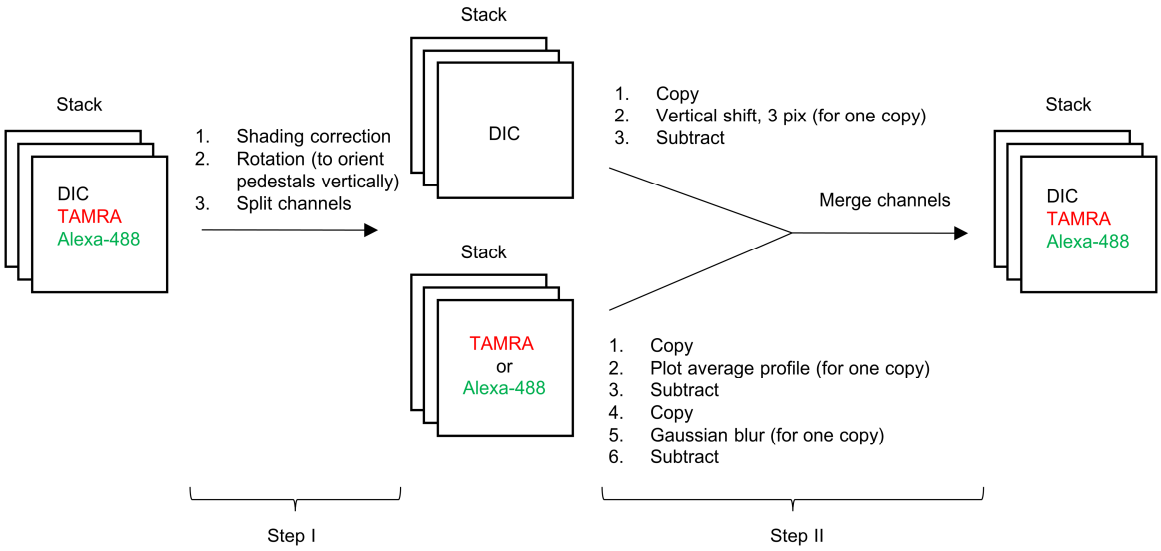

Figure S6. Schematic representation of an algorithm for correcting flare from pedestals in DIC and fluorescence

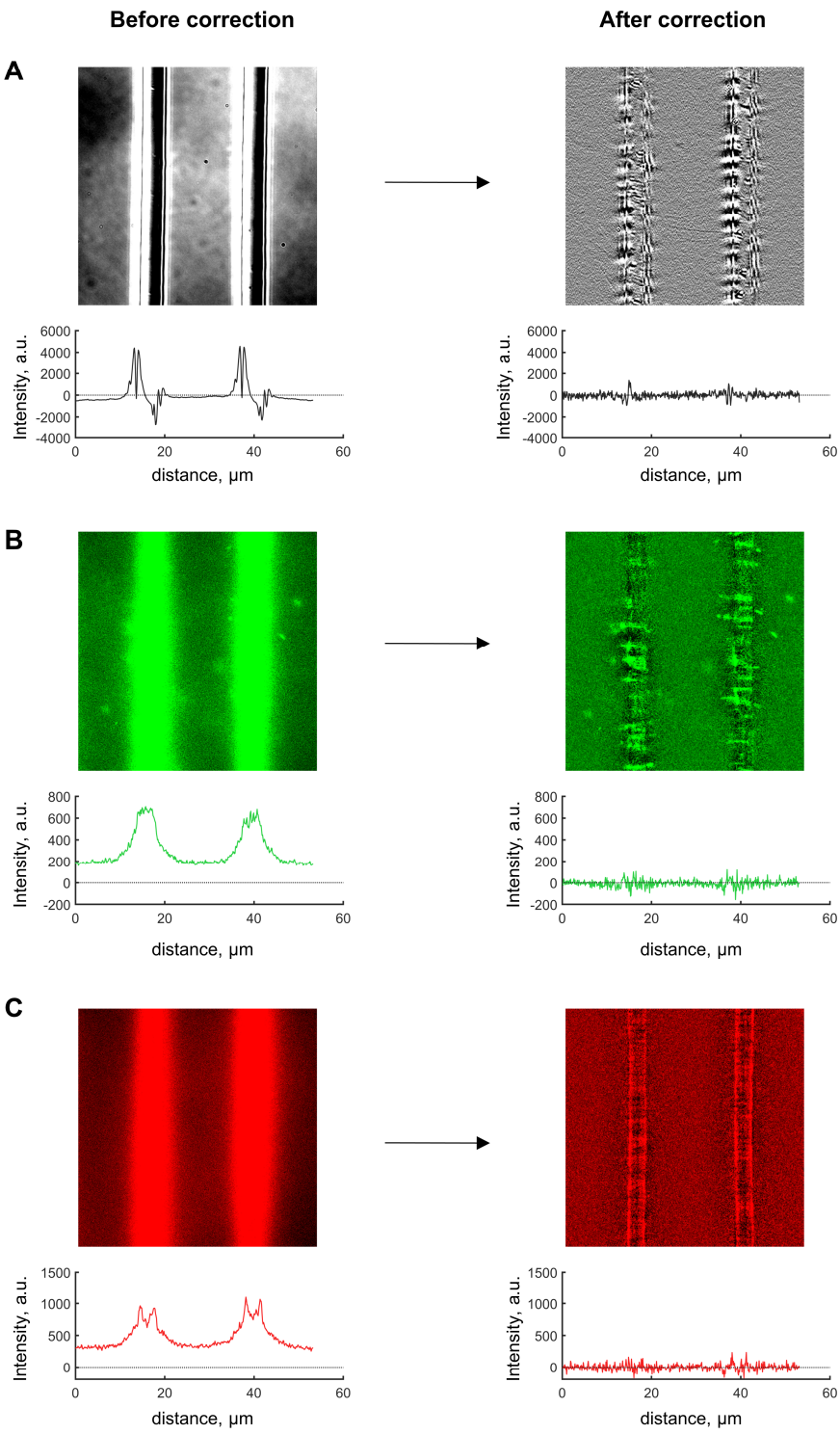

Figure S7. Examples of application of the pedestal flare correction algorithm for DIC and fluorescence. All Images show a field with pedestals before and after the flare correction, the graphs below the images show corresponding intensity profiles. (A) DIC channel. (B) Green fluorescent channel. (C) Red fluorescent channel.

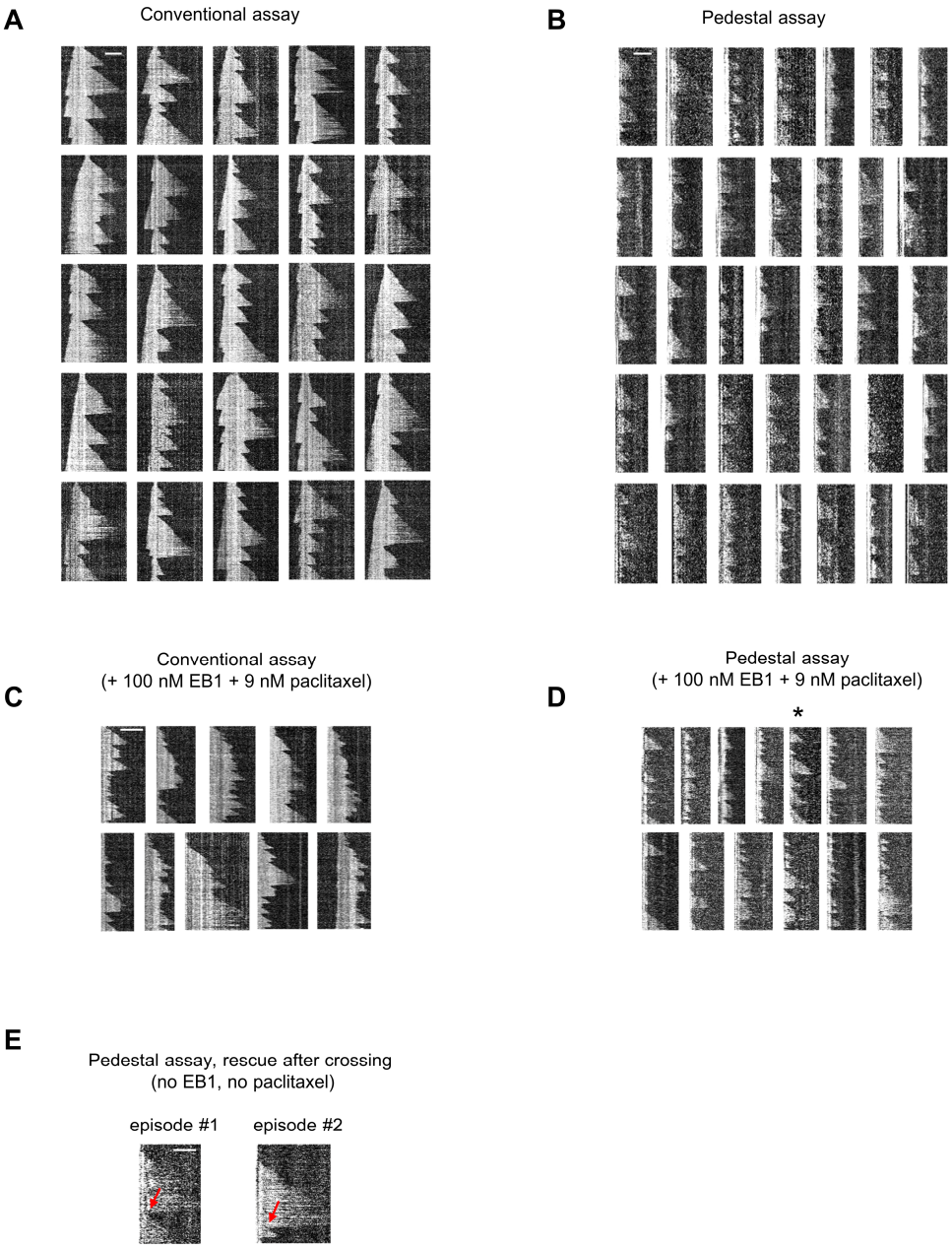

Figure S8. Representative kymographs of microtubule dynamics. Scale bars are 5 μm. (A) Conventional assay with 17 μM tubulin. (B) Modified (pedestal) assay with 17 μM tubulin. (C) Conventional assay with 17 μM tubulin, 100 nM EB1 and 9 nM paclitaxel. (D) Modified (pedestal) assay with 17 μM tubulin 100 nM EB1 and 9 nM paclitaxel. Asterisk marks the kymograph, corresponding to the microtubule tracked in Video S10. (E) Kymographs, corresponding to the crossing microtubules, tracked in Video S8. Red arrows point to rescues.

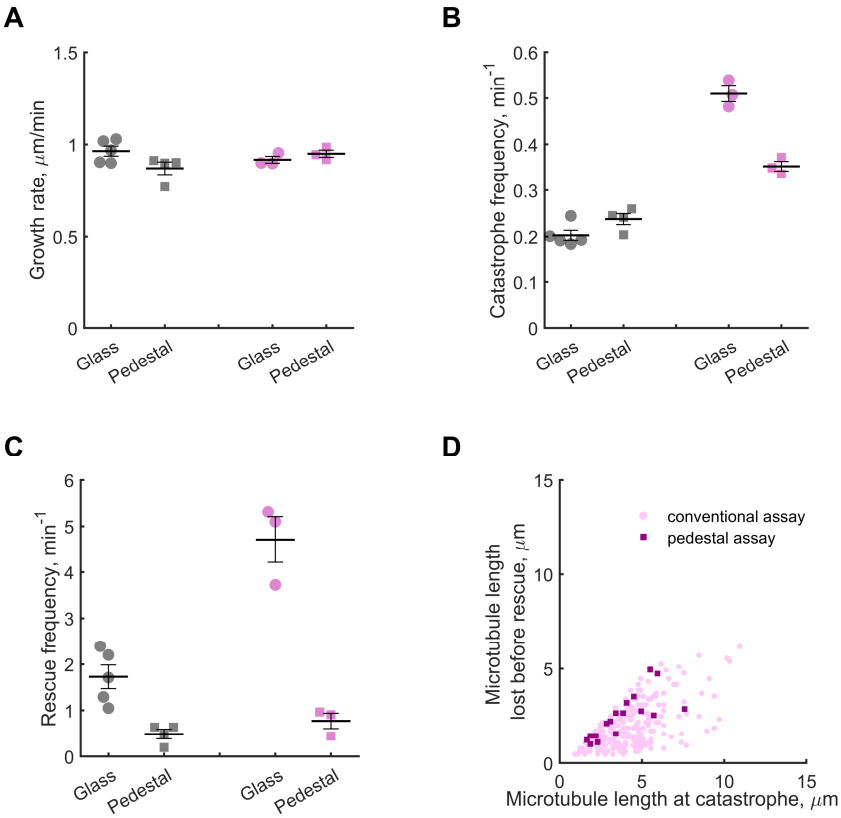

Figure S9. Parameters of microtubule dynamics in the conventional and the pedestal assays in presence of EB1 and paclitaxel. In panels A-C data from measurements without EB1 and paclitaxel are reproduced from Fig 4 for convenience of comparison (gray). Data in presence of EB1 and paclitaxel are shown in magenta in all panels (A) Average microtubule growth rate in the conventional (coverslip) and the modified (pedestal) assays in presence or absence of 100 nM EB1 and 9 nM paclitaxel. Each point corresponds to an independent experiment. (B) Average catastrophe frequency in the conventional (coverslip) and the modified (pedestal) assays in presence or absence of 100 nM EB1 and 9 nM paclitaxel. Each point corresponds to an independent experiment. (C) Average rescue frequency in the conventional (coverslip) and the modified (pedestal) assays in presence or absence of 100 nM EB1 and 9 nM paclitaxel. Each point corresponds to an independent experiment. (D) Dependence of the rescue positions in the conventional (pale circles) and the pedestal (dark squares) assays on the microtubule length at catastrophe.

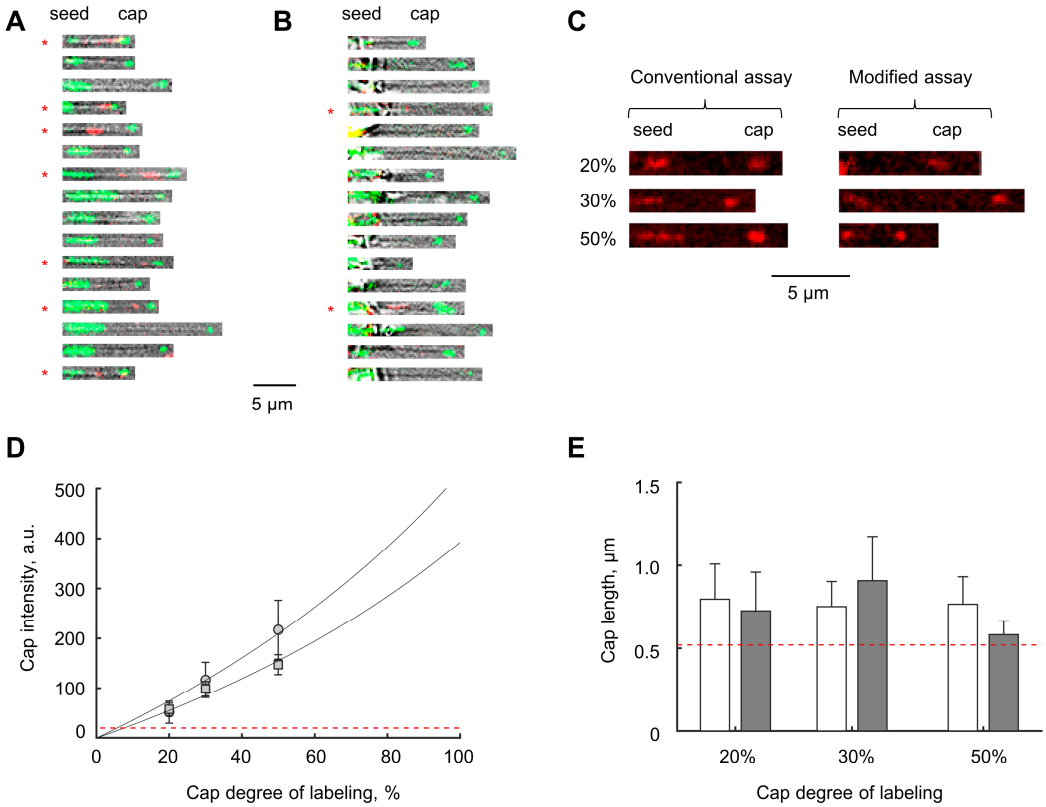

Figure S10. Extended data on GTP-tubulin incorporation into microtubule shaft in the conventional and the modified assay. (A) A gallery of microtubule images in DIC and two fluorescent channels, visualizing the TAMRA-labeled tubulins, incorporated into microtubule shaft in the conventional assay. Red asterisks mark examples with TAMRA-tubulin islands. (B) A gallery of microtubule images in DIC and two fluorescent channels, visualizing the TAMRA-labeled tubulins, incorporated into microtubule shaft in the modified (pedestal) assay. (C) Images of TAMRA-labeled GMPCPP caps, on microtubules, nucleated from TAMRA-labeled GMPCPP-seeds in conventional and modified (pedestals) assay. The degree of labeling of TAMRA-tubulin in the GMCPP cap is varied: 20%, 30% and 50%. (D) Quantification of the sensitivity of TAMRA-tubulin island detection in the conventional and the modified assay, based on data illustrated in panel C. Circles show data from the conventional assay, squares show data from the pedestal assay. Red line marks the level, corresponding to the standard deviation of the background noise. (E) Quantification of the size TAMRA-labeled GMPCPP caps. White and gray bars correspond to the mean cap sizes in the conventional and pedestal assays, respectively. Error bars are standard deviations. Red line corresponds to the minimal size of the TAMRA-tubulin island, detected in the conventional assay.

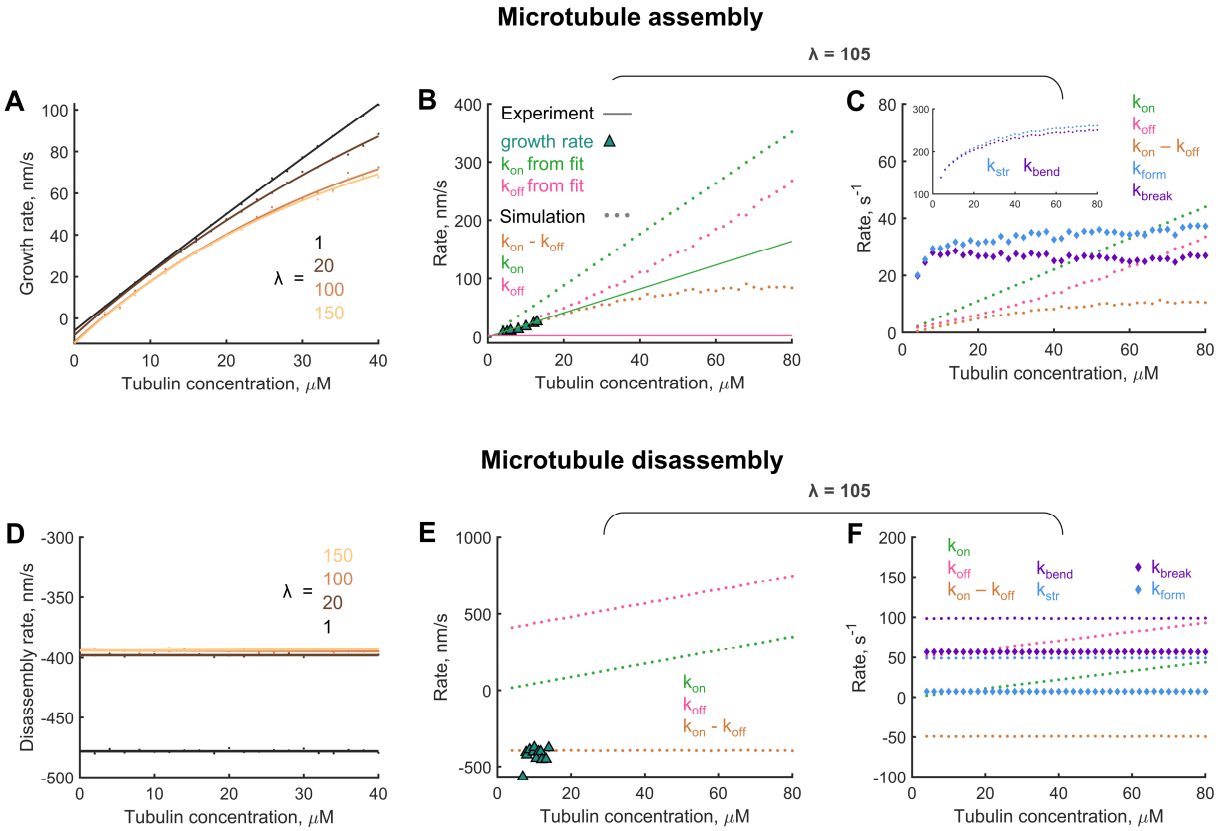

Figure S11. Interplay between kinetic processes during microtubule assembly and disassembly in the simulations. (A) Microtubule growth rate vs. tubulin concentration for different kinetic penalties for straightening the curved lagging protofilaments. When the penalty (λ) is high, the growth rate is predicted to deviate from a linear dependence at high tubulin concentrations. (B) Dotted lines show tubulin association rate (k_{on}), dissociation rate (k_{off}) and their net difference in the calibrated model (expressed in nm/s) as functions of the soluble tubulin concentration. Here and in other panels of this figure k_{off} is reported as the average number of tubulin dimers dissociating from the microtubule tip per second. As the bent protofilaments can break at any position, the average dissociation rate is tubulin-concentration-dependent. The green triangles and the solid green and pink lines show experimental data (2) with a linear fit, respectively. (C) Dotted lines show association rate (k_{on}), dissociation rate (k_{off}) and their difference in the calibrated model (repeated from panel B, but now expressed in s^{-1}) as functions of the soluble tubulin concentration. Blue and purple diamonds show the averaged rates of the lateral bond formation and breakage in the simulations vs. tubulin concentration, respectively. The inset shows analogous dependences for tubulin dimer straightening and bending rates. At low and medium tubulin concentrations, the microtubule growth rate is limited by the association rate constant (k_{on}). At higher tubulin concentrations, the growth rate starts deviating from the linear curve when the rate of the lateral bonds formation (k_{form}) becomes comparable to k_{on}. (D) Microtubule disassembly rate vs. tubulin concentration for different kinetic penalties for straightening the curved lagging protofilaments. (E) Dotted lines show tubulin association rate (k_{on}), dissociation rate (k_{off}) and their difference in the calibrated model (expressed in nm/s) are shown as functions of the soluble tubulin concentration during microtubule disassembly. The green triangles show experimental data (3). (F) Dotted lines show the association rate (k_{on}, green), the dissociation rate (k_{off}, pink), their net difference (k_{on} - k_{off}, orange), the tubulin straightening rate (k_{str}, blue), and the tubulin bending rate (k_{bend}, magenta) as functions of the soluble tubulin concentration during microtubule disassembly. Blue and purple diamonds show the averaged rates of the lateral bond formation and breakage in the simulations vs. tubulin concentration, respectively. The overall microtubule shortening rate is limited by the rate of lateral bond breakage.

Supplementary Video Legends

Video S1. Simulated microtubule growth with different parameters with GTP hydrolysis off and on. The video panels correspond to the middle curves in each of the six panels of Fig S2. GDP-tubulins are shown in green, GTP-tubulins are red. Black dots mark the termini of the protofilaments to make the tips of the protofilaments more clearly visible. Every 500-th iteration of the simulation is shown in the video at 60 frames per second.

Video S2. Destabilization of microtubule growth by lagging curved protofilaments (high activation barrier case), shown in the 'slow motion' mode. Microtubule is assembled at 10 μM tubulin. Until the 382-nd second of the video every 500-th iteration of the simulation is displayed at 60 frames per second. Starting from the 382-nd second of the simulated time, when the microtubule approaches a catastrophe, the time resolution of the video is increased 50-fold for better visualization of events triggering a catastrophe. GDP-tubulins are shown in green, GTP-tubulins are red. Black dots mark the termini of the protofilaments to make the tips of the protofilaments more clearly visible.

Video S3. Destabilization of microtubule growth by lagging curved protofilaments (high activation barrier case). Example simulations at three tubulin concentrations are shown: 5 μM, 8 μM and 11 μM. GDP-tubulins are shown in green, GTP-tubulins are red. Black dots mark the termini of the protofilaments to make the tips of the protofilaments more clearly visible. Every 500-th iteration of the simulation is shown in the video at 60 frames per second.

Video S4. Simulation of the tubulin dilution experiment. Microtubules are elongating at 10 μM tubulin for 35 s, tubulin concentration is then set to 0 μM. GDP-tubulins are shown in green, GTP-tubulins are red. Black dots mark the termini of the protofilaments to make the tips of the protofilaments more clearly visible. Every 500-th iteration of the simulation is shown in the video at 60 frames per second.

Video S5. Simulation of microtubule disassembly past a GTP-tubulin island (3x4 dimers). The average probability to rescue in this case is 8%. Two examples are shown: with and without a rescue. GDP-tubulins are shown in green, GTP-tubulins are red. Black dots mark the termini of the protofilaments to make the tips of the protofilaments more clearly visible. Every 500-th iteration of the simulation is shown in the video at 60 frames per second.

Video S6. Visualization of microtubule dynamics in the conventional in vitro assay. Microtubule dynamics is visualized with DIC microscopy. The white arrow is pointing to the plus end of a GMPCPP seed, attached to the coverslip. The green arrow is pointing to the rescue position in the microtubule shaft. Video is played 3.3 times faster than real time.

Video S7. Visualization of microtubule dynamics in the pedestal assay. Microtubule dynamics is visualized with DIC microscopy. In the beginning of the video, the white arrow is pointing to the plus end of a GMPCPP seed, attached to a microfabricated pedestal, and continues to track the dynamic plus end of the microtubule, growing from the seed. The video has been processed to correct the flare around the pedestal (see Supplementary Methods). The playback speed is 3.3 times faster than real time.

Video S8. Visualization of rescues of crossing microtubules in the pedestal assay. Dynamics of two crossing microtubules are visualized with DIC microscopy. In both cases (episode #1 and #2) the same field of view is shown. The red arrow is pointing at the microtubules' intersection. The green arrow is pointing to the position, where one of the crossing microtubules undergoes rescue. Both microtubules are growing from plus ends of the GMPCPP seeds, attached to a microfabricated pedestal, however the ends of the seeds do not extend beyond the edge of the pedestal. Two rescues are visible near the pedestal edge (please, also see the corresponding kymographs in Fig S8E). The video has been processed to correct the flare around the pedestal (see Supplementary Methods). The playback speed is 3.3 times faster than real time.

Video S9. Visualization of microtubule dynamics in the conventional in vitro assay in the presence of EB1 and paclitaxel. Microtubule dynamics is visualized with DIC microscopy. The white arrow is pointing to the plus end of a GMPCPP seed, attached to a coverslip. The green arrow highlights the rescue positions

in the microtubule shaft. Each of the rescues is located not closer than 0.5 μm from the plus end of the GMPCPP seed. The video is played 3.3 times faster than real time.

Video S10. Visualization of microtubule dynamics in the pedestal assay in the presence of EB1 and paclitaxel. Microtubule dynamics is visualized with DIC microscopy. In the beginning of the video, the white arrow is pointing to the plus end of a GMPCPP seed, attached to a microfabricated pedestal, and it continues to track the dynamic plus end of the microtubule, growing from the seed. The kymograph of the tracked microtubule is shown in Fig S8D (marked with an asterisk). Video has been processed to correct the flare around the pedestal (see Supplementary Methods). The playback speed is 3.3 times faster than real time.

.